ADVANCED MATERIALS
www.advmat.de

Achieving Ultrahigh-Rate Planar and Dendrite-Free Zinc Electroplating for Aqueous Zinc Battery Anodes

Shengda D. Pu, Chen Gong, Yuanbo T. Tang, Ziyang Ning, Junliang Liu, Shengming Zhang, Yi Yuan, Dominic Melvin, Sixie Yang, Liquan Pi, John-Joseph Marie, Bingkun Hu, Max Jenkins, Zixuan Li, Boyang Liu, S. C. Edman Tsang, T. James Marrow, Roger C. Reed, Xiangwen Gao, Peter G. Bruce,* and Alex W. Robertson**

Despite being one of the most promising candidates for grid-level energy storage, practical aqueous zinc batteries are limited by dendrite formation, which leads to significantly compromised safety and cycling performance. In this study, by using single-crystal Zn-metal anodes, reversible electrodeposition of planar Zn with a high capacity of 8 mAh cm^{-2} can be achieved at an unprecedentedly high current density of 200 mA cm^{-2}. This dendrite-free electrode is well maintained even after prolonged cycling (>1200 cycles at 50 mA cm^{-2}). Such excellent electrochemical performance is due to single-crystal Zn suppressing the major sources of defect generation during electroplating and heavily favoring planar deposition morphologies. As so few defect sites form, including those that would normally be found along grain boundaries or to accommodate lattice mismatch, there is little opportunity for dendritic structures to nucleate, even under extreme plating rates. This scarcity of defects is in part due to perfect atomic-stitching between merging Zn islands, ensuring no defective shallow-angle grain boundaries are formed and thus removing a significant source of non-planar Zn nucleation. It is demonstrated that an ideal high-rate Zn anode should offer perfect lattice matching as this facilitates planar epitaxial Zn growth and minimizes the formation of any defective regions.

1. Introduction

The aqueous zinc battery's (AZB) low cost, eco-efficiency, safety, and high volumetric capacity make it particularly attractive for future grid-level energy storage applications. Metallic Zn, as the ideal anode for AZBs, has the highest theoretical capacity (5851 mAh mL^{-1}). It is also non-toxic, non-flammable, abundant, and has good electrical conductivity and water stability.[1–5] However, conventional metallic Zn anodes suffer from severe dendrite formation during cycling, causing serious problems like poor reversibility, voltage hysteresis, increased parasitic reactions, shorting-induced battery failures, and other issues.[1,3,6] These dendritic structures, either rarefied needle, or non-planar platelet deposits, preferentially form at irregular or defective areas of the electrode where the localized current density is highest and the initial nucleation event is most likely,[7] and is exacerbated by cycling at high current densities and capacities.[8,9] Strategies for controlling and suppressing dendritic growth have revolved around manipulating the electrolyte, typically by inclusion of additives,[10–15] or by engineering the electrode into a high-surface-area sponge,[16–18] or with a protective surface coating,[19] in order to suppress dendrite formation.

S. D. Pu, C. Gong, Y. T. Tang, Z. Ning, J. Liu, S. Zhang, Y. Yuan, D. Melvin, S. Yang, L. Pi, J.-J. Marie, B. Hu, M. Jenkins, Z. Li, B. Liu, T. J. Marrow, R. C. Reed, X. Gao, P. G. Bruce, A. W. Robertson
Department of Materials
University of Oxford
Parks Road, Oxford OX1 3PH, UK
E-mail: xiangwen.gao@materials.ox.ac.uk; peter.bruce@materials.ox.ac.uk; alex.w.robertson@warwick.ac.uk

J.-J. Marie, P. G. Bruce
The Faraday Institution
Quad One
Becquerel Avenue
Harwell Campus
Didcot OX11 0RA, UK

The ORCID identification number(s) for the author(s) of this article can be found under https://doi.org/10.1002/adma.202202552.

DOI: 10.1002/adma.202202552

S. C. E. Tsang
The Wolfson Catalysis Centre
Department of Chemistry
University of Oxford
South Parks Road, Oxford OX1 3QR, UK

R. C. Reed
Department of Engineering Science
University of Oxford
Parks Road, Oxford OX1 3PJ, UK

P. G. Bruce
Department of Chemistry
University of Oxford
South Parks Road, Oxford OX1 3QZ, UK

P. G. Bruce
The Henry Royce Institute
Parks Road, Oxford OX1 3PH, UK

A. W. Robertson
Department of Physics
University of Warwick
Coventry CV4 7AL, UK

Rather than attempting to mechanically or structurally limit dendrite formation, an alternative approach is to incentivize planar Zn deposition and growth, as a flat anode morphology is ideal for preventing dendrites and for achieving high cycling reversibility.[20] This can be achieved via the controlled deposition of (002)-orientated Zn; the (002) Zn face is the lowest surface energy face at 0.02 eV $Å^{-2}$, nearly three times lower than that of the (111) and (101) faces,[21] facilitating the deposition of flat Zn platelets that plate parallel to the anode surface. Several strategies have been employed to harness the improved performance offered by this preferential planar Zn deposition process, including etching or rolling the metal anode to primarily exhibit the (002) face texture,[22–24] or by manipulating the electrolyte chemistry to favor (002) Zn deposition.[25–27] Recent studies have shown that using anodes with a semi-matching crystal lattice to that of Zn, for example graphene or Sn,[28–31] can also induce preferential Zn electrodeposition along the (002) orientations,[32] and their reduced nucleation barrier helped foster evenly distributed nucleation events and a more uniform plated surface.[29,30] Yet non-planar structures were still observed with these innovative Zn anodes, particularly around the grain boundaries and island edges of the electrodeposited Zn.[28,29] Once such non-planar deposits form they disturb the homogenous landscape of the initial anode surface, impairing the preference toward uniform planar plating upon subsequent cycling,[29] and thus ultimately limiting the electrode's ability to cycle repeatedly at high rates. We therefore require an anode material that facilitates planar Zn electroplating with minimal defects, and thus minimal available nucleation sites for dendritic and non-planar Zn deposition,[28–30,33] if we are to safely attain high charging rates in Zn batteries.

Here, we demonstrate how defect-suppression can yield exceptional performance by employing single-crystal (002) Zn as an ideal model anode. The lack of grain boundaries in the single-crystal, the perfect homoepitaxial lattice matching with plated Zn, and the sole expression of only the (002) face, effectively excludes the formation of the defective regions that act as the nucleation sites for irregular Zn deposition, instead yielding uniformly flat plating that permits repeatable cycling at high rates of up to 200 mA cm^{-2}. A flat anode surface was well maintained after 1200 cycles (at 4 mAh cm^{-2} per cycle) with minimal capacity loss, translating to an average coulombic efficiency (CE) of 99.94%. We have also demonstrated how this planar plating system can be used as a new, low-cost method to produce high-quality, high-density Zn single crystal at scale.

2. Results and Discussion

Electroplating was performed on the (002) surface of polished single-crystal Zn ("Single-Zn") with 2 M $ZnSO_4$ aqueous electrolyte, which has been reported to have good electrochemical performance and to be less hazardous.[34,35] For comparison, other substrate materials—316 stainless steel, copper, platinum, polycrystalline Zn ("Poly-Zn")—were also electroplated with Zn under the same conditions (capacity: 0.5 mAh cm^{-2}; current density: 2 mA cm^{-2}). Experimental details are described in the methods. Inspection of the deposition by scanning electron microscopy (SEM) revealed the Zn deposited on stainless steel, copper, platinum, and Poly-Zn all exhibited a randomly orientated, flaky morphology that frequently extended outward from the electrode surface (**Figure 1**a–d and Figures S1, S2, Supporting Information). These irregular structures led to severe roughening of the electrode, as shown by atomic force microscopy (AFM) imaging (Figure 1i,j). These highly uneven deposition morphologies will facilitate dendrite growth upon further plating or cycling.[2,8,36] In comparison, Zn plated on the Single-Zn electrodes produced flat and smooth hexagonal islands that all exhibited the same rotational alignment (Figure 1e,f,k). The electrodeposition interface was examined using SEM coupled with focused ion beam (FIB) cross-sectioning and energy-dispersive X-ray spectroscopy (EDS) mapping (Figure 1g,h and Figure S3, Supporting Information), which revealed no distinguishable defects or any C or O segregation (common inclusion containing elements) between the electroplated Zn and the substrate Zn. These interfacial qualities, along with the rotational alignment of the hexagons, strongly suggest that the Zn islands formed coherent, epitaxial metallic bonds with the Single-Zn substrate. The same planar deposition morphology was also observed when 2M $Zn(CF_3SO_3)_2$ aqueous electrolyte was used (Figure S4, Supporting Information).

To ascertain the performance limits of the Single-Zn electrode, we examined its electroplating performance under higher capacities and current densities, conditions under which Zn anodes are known to be more susceptible to dendrite formation.[8,9] As we increased the plating current density from 2 to 10 mA cm^{-2} and the plating capacity from 1 to 8 mAh cm^{-2}, the layered planar Zn deposition was perfectly maintained (**Figure 2**a). To confirm the plated crystal orientation we employed extended field-of-view electron backscatter diffraction (EBSD), which can acquire a crystallographic map of a sample's surface. EBSD mapping requires a flat specimen, typically polished smooth, and thus is not usually suitable for characterization of electrodes post-plating. However, as our Single-Zn electrodes were uniformly plated with smooth planar Zn, we were able to perform EBSD, which confirmed that the plated Zn only exhibited one crystal orientation, matching that of the underlying Single-Zn substrate (Figure S5, Supporting Information). While keeping the plating capacity at 8 mAh cm^{-2} we further increased the electroplating current density. It was found that the electroplated Zn remained planar with no dendrite growth even under an ultrahigh electroplating current density of 200 mA cm^{-2} (Figure 2b), a record that has not been reported in AZBs or any other battery systems without employing porous 3D anodes.[37,38] (A 3D scaffold can substantially reduce the effective local current density and areal capacity felt by the anode during electroplating or cycling due to its significantly higher effective surface in contact with the electrolyte, creating a cycling condition that is less prone to dendrite formation, with the drawbacks of having a lower energy density and being potentially suceptible to different failure mechanisms).

X-ray diffraction (XRD) and extended field-of-view EBSD mapping were employed to further assess the quality of the plated Zn. XRD was acquired directly from the electrodes following electrodeposition to 8 mAh cm^{-2} capacity. The XRD pattern remained unchanged after plating at either 10 or 200 mA cm^{-2} (Figure 2d), proving that minimal non-planar Zn formed during the electrodeposition. In comparison,

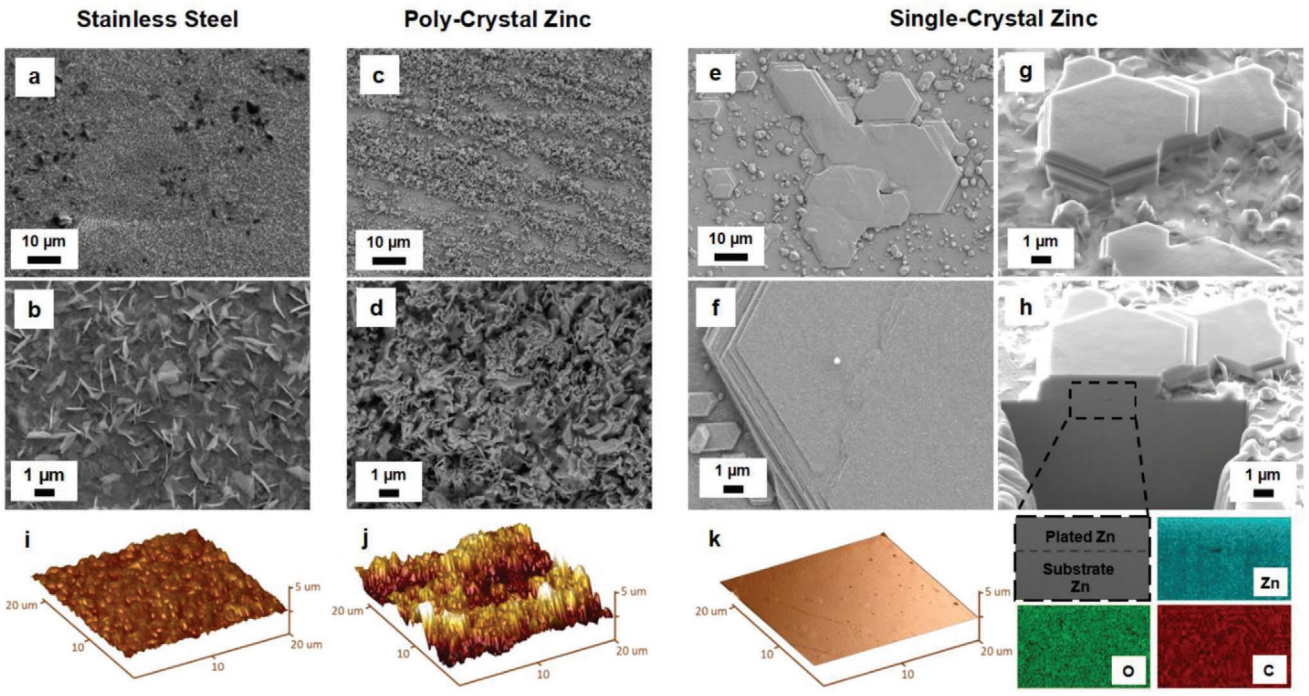

Figure 1. Morphology of electroplated zinc on different anode substrates. a–f) Low- and high-magnification SEM images of Zn electroplated on stainless steel (a,b), Poly-Zn (c,d), and Single-Zn (e,f). g,h) Cross-sectional SEM imaging and EDS mapping of the interface between electroplated Zn and the Single-Zn substrate (total EDS counts: C K$\alpha = 2.0 \times 10^5$; O K$\alpha = 2.2 \times 10^5$; Zn L$\alpha = 2.3 \times 10^6$). i–k) AFM surface profiles of zinc plated on stainless steel (i), Poly-Zn (j), and Single-Zn (k).

electroplating on stainless steel, copper and Poly-Zn all resulted in significant Zn growth along other crystal orientations, including (100), (101), and (110), which are known to be more susceptible to dendrite formation and corrosion.[32] A Cu signal is visible due to the especially irregular plating morphology, leaving significant bare Cu surface still exposed even after plating to 8 mAh cm^{-2}. Extended field-of-view EBSD mapping (Figure 2e, Figures S6, S7, Supporting Information) further confirmed that electroplating on Single-Zn was consistently planar across the entire electrode, exhibiting only the (002) crystal orientation.

It was also found that electroplating on Single-Zn anodes yielded Zn islands that could seamlessly merge into larger single grains during extended electroplating, with no grain boundaries or inter-grain defects. This phenomenon can be qualitatively observed in the microscopy images of Zn plated under 200 mA cm^{-2} (Figure 2c), where multiple individual hexagonal pyramidal Zn islands were formed due to the ultrafast plating kinetics. These hexagonal planar islands maintained uniform rotational alignment. The step edges of these islands continued to favor planar island growth due to sharing the same (002) orientation as the substrate. The mergence interface of these islands was inspected by cross-sectional SEM and EBSD mapping (Figure 2f–h). The FIB-milled cross-section (Figure 2g) showed no significant cracking or void formation at the interface between the two islands upon mergence. This 21 μm deep cross-section also revealed the exceptional plating quality of the Zn metal at this high current density, with no internal occlusions or defects. EBSD mapping at the triple point between three merged Zn islands (Figure 2h) further confirms that no out-of-plane Zn crystal orientation formed at the interface upon mergence and no twinning was generated to accommodate any lattice mismatch, as shown by the uniform color distribution along all three directions. These results strongly suggest that the electroplated Zn islands are able to merge into single grains with perfectly matched atomic stitching linking them together.

Our results show how using an anode with a perfect-matched lattice to Zn allows for excellent high-rate performance well beyond that achievable by other substrates. This is due to two key advantages: i) with a single-crystal Zn anode, a stress-free interface can be well-maintained along the entire (002) crystal plane throughout plating. The stress-free, homoepitaxial Zn-on-Zn plating offers the lowest energy barrier and thus is optimal for epitaxial planar Zn growth. This is evidenced by the low nucleation overpotential for plating on Single-Zn, as well as the mass transport limit not being reached even at plating currents up to 250 mA cm^{-2} (Figure S8, Supporting Information). ii) The uniform orientation of the substrate, due to being single crystal, and its perfect lattice matching with the Zn deposit, allow individual plated islands to merge together into a larger single grain, maintaining perfect inter-grain atomic stitching upon mergence (**Figure 3**). After the initial nucleation (Figure 3i,l,p), these discrete hexagonal Zn islands uniformly thicken and expand (Figure 3j,m,q), and eventually merge together into a single grain upon extended electroplating (Figure 3n,r), as confirmed by EBSD (Figure 2e). Semi-matched substrates (Figure 3a–g), however, may form imperfect interfaces due to the Zn-substrate lattice mismatch, as two Zn islands may not form a perfect hexagonal closed-pack (HCP) lattice structure upon encounter (Figure 3c, insert): Atom A from island 1 will bond with atom B from island 2, but not atom C or D due to the inter-atomic distance. The lattice mismatch prevents

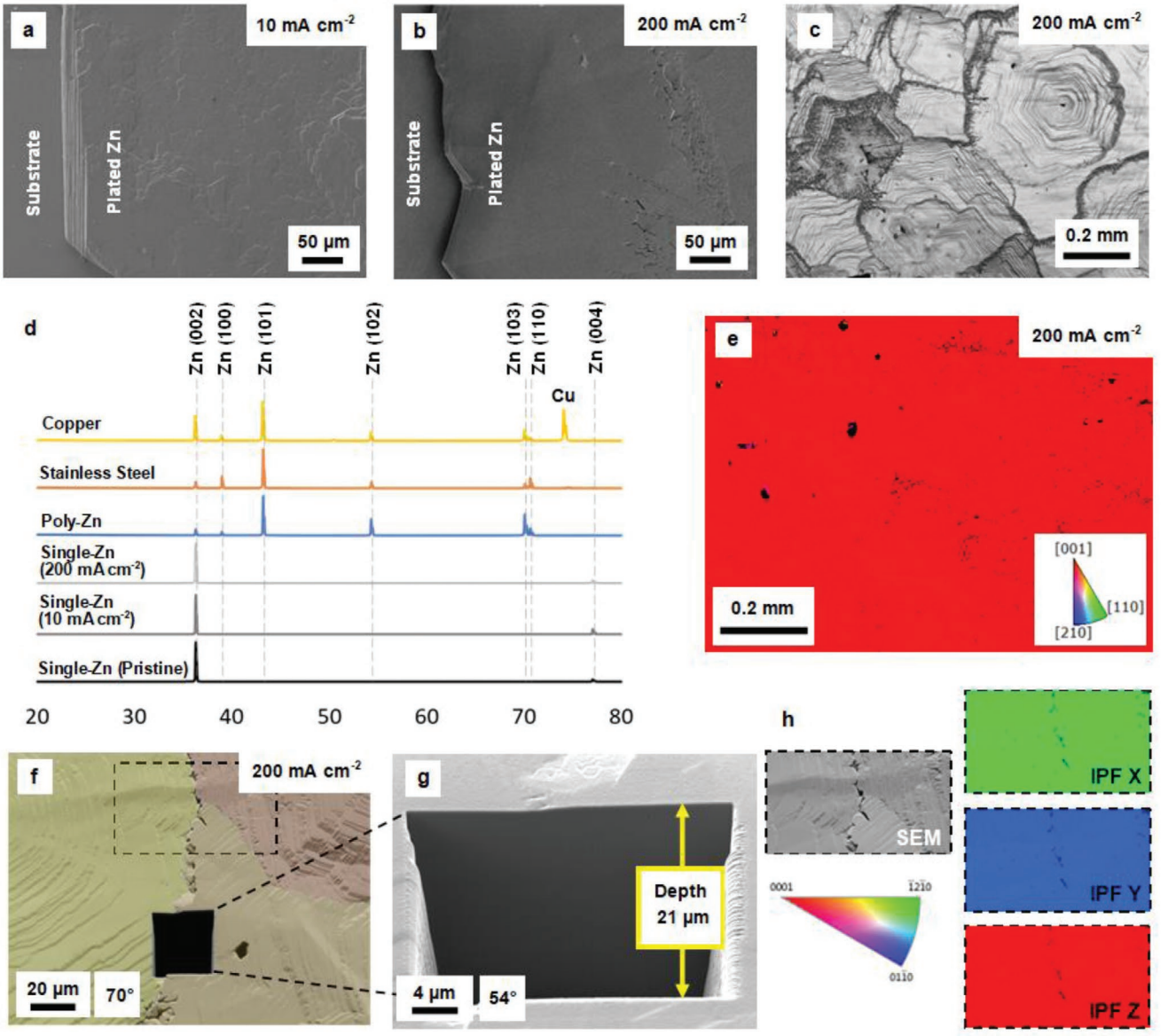

Figure 2. High-rate Single-Zn electroplating. a,b) SEM images of Zn electroplated to Single-Zn electrode at 10 mA cm^{-2} (a) and 200 mA cm^{-2} (b). Part of the substrate surface was blocked during plating to allow for comparison between the electroplated Zn and the Single-Zn surface (see methods). c) Low-magnification optical microscopy image of Zn electroplated to Single-Zn electrode at 200 mA cm^{-2}. d) XRD of the electroplated Zn on various electrode substrates. e) Low-magnification EBSD orientation map of Single-Zn electrode after 200 mA cm^{-2} Zn plating. f) SEM image of three merged electroplated Zn islands on Single-Zn. g) SEM image of an FIB cross-section through the interface between two merged Zn islands (the dark square in (f)). h) EBSD orientation maps acquired from across the intersection of three islands (the dashed region in (f)). All plating experiments were performed to a capacity of 8 mAh cm^{-2}.

them from forming a perfect hexagon-shaped HCP (002) basal plane at their interface. This imperfect interface, that is, a grain boundary, will lead to defective regions forming in between these islands, that is, grains,[39–42] leaving them susceptible to other side-reactions and non-planar Zn growth, as evidenced in previous studies on semi-matched substrates.[28–30] Such defect and dendrite formation induced by an imperfect interface have been reported in other metallic anode battery systems.[43,44] The strong preference toward planar island morphologies when electroplating on to the Zn (002) surface, due to the low-surface-energy facet favoring lateral growth, well complements the inter-island stitching behavior of our single-crystal anode.

To confirm that this perfect epitaxial deposition is not only well maintained after a single electroplating but also over prolonged cycling, we conducted further electrochemical evaluation of the Single-Zn anode's cycling performance. A Single-Zn symmetric cell was cycled for 100 cycles at a current density of 10 mA cm^{-2} with 1 mAh cm^{-2} capacity, a test condition commonly used in AZB studies,[6,8,45] and for comparison a Poly-Zn/stainless-steel cell and a Poly-Zn symmetric cell were cycled under the same conditions (**Figure 4**a, Figures S7, Supporting Information). The Poly-Zn/stainless-steel cell developed a significant plating overpotential after only 30 cycles (Figure 4a), and large amounts of electrically isolated "dead

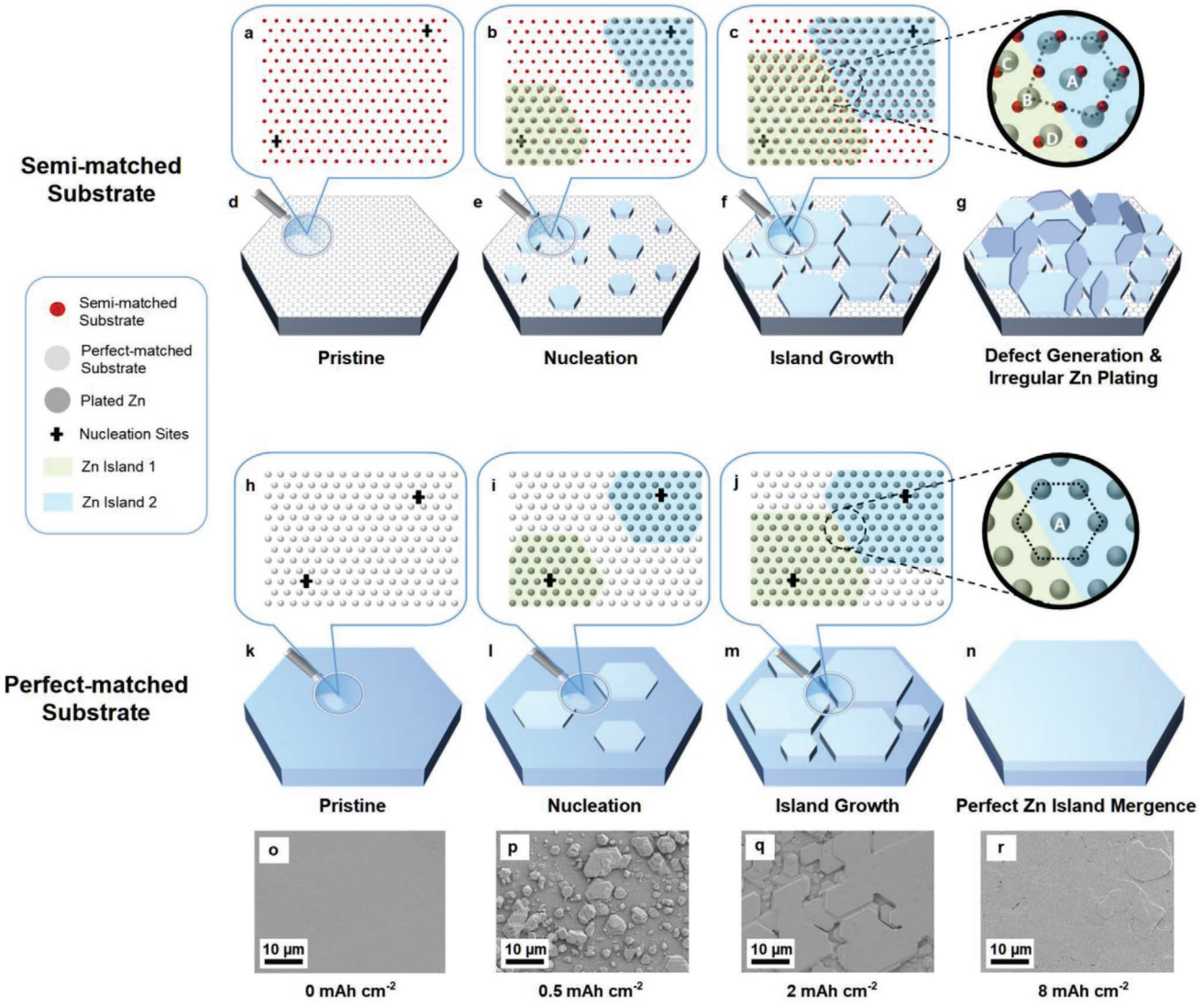

Figure 3. Comparison of Zn electroplating sequences on different substrates. a–g) Electroplating Zn to a semi-matched substrate, with magnified inserts in (a–c) illustrating atomic arrangements and defective grain boundary formation, and in (d–g) the morphological evolution. h–n) Electroplating to a perfect-matched substrate, with magnified inserts in (h–j) illustrating atomic arrangements and inter-island stitching, and in (k–n) the morphological evolution. o–r) SEM of electroplated Zn on a Single-Zn anode at increasing capacities at 2 mA cm^{-2} plating rate.

Zn"[36] were found in the separator after disassembling the cell (Figure 4a, inset i), indicating Zn dendrite formation and detachment during cycling. In comparison, no sign of "dead Zn" was found on the separator of the Single-Zn symmetric cell after cycling (Figure 4a, inset ii). By titrating the separators with H_2SO_4 solution and detecting H_2 evolution via on-line mass spectrometry,[46,47] we quantified the residual "dead Zn" in the Poly-Zn/stainless-steel cell and the Poly-Zn symmetric cell to be 0.73 and 0.032 mAh cm^{-2}, while no hydrogen evolution signal indicative of "dead Zn" was picked up from the Single-Zn symmetric cell (Figure 4a, inset iii, and Figure S10, Supporting Information). And despite some localized grooving observed on the metal surface, the Single-Zn anode perfectly maintained its planar (002) crystal orientation after cycling, as confirmed by XRD and post-cycling EBSD, and showed no sign of dendrite formation (Figure 4d, Figure S11, Supporting Information). The resultant surface grooving was most likely due to non-uniform stripping events which can lead to the formation of localized pits on the surface, as observed in a Single-Zn anode after stripping (Figure S12, Supporting Information).

Even when cycled at a higher rate of 50 mA cm^{-2} and higher capacity of 4 mAh cm^{-2} for 1200 cycles, the planar anode surface was well maintained (Figure 4f) and no significant plating/stripping overpotential increase was observed (Figure 4c). Since conventional electrochemical tests, employing either a Zn/stainless-steel or a Zn/Zn symmetric cell, cannot be used to measure the reversibility and efficiency of the Single-Zn anode due to its excess capacity,[48] here we instead used its mass loss over cycling to quantify capacity loss. The mildly acidic AZB yields minimal electrochemical side-reactions, and thus forms a minimal solid-electrolyte interphase (SEI) during cycling,[1,2,49,50] as confirmed by cyclic voltammetry (Figure 4b,

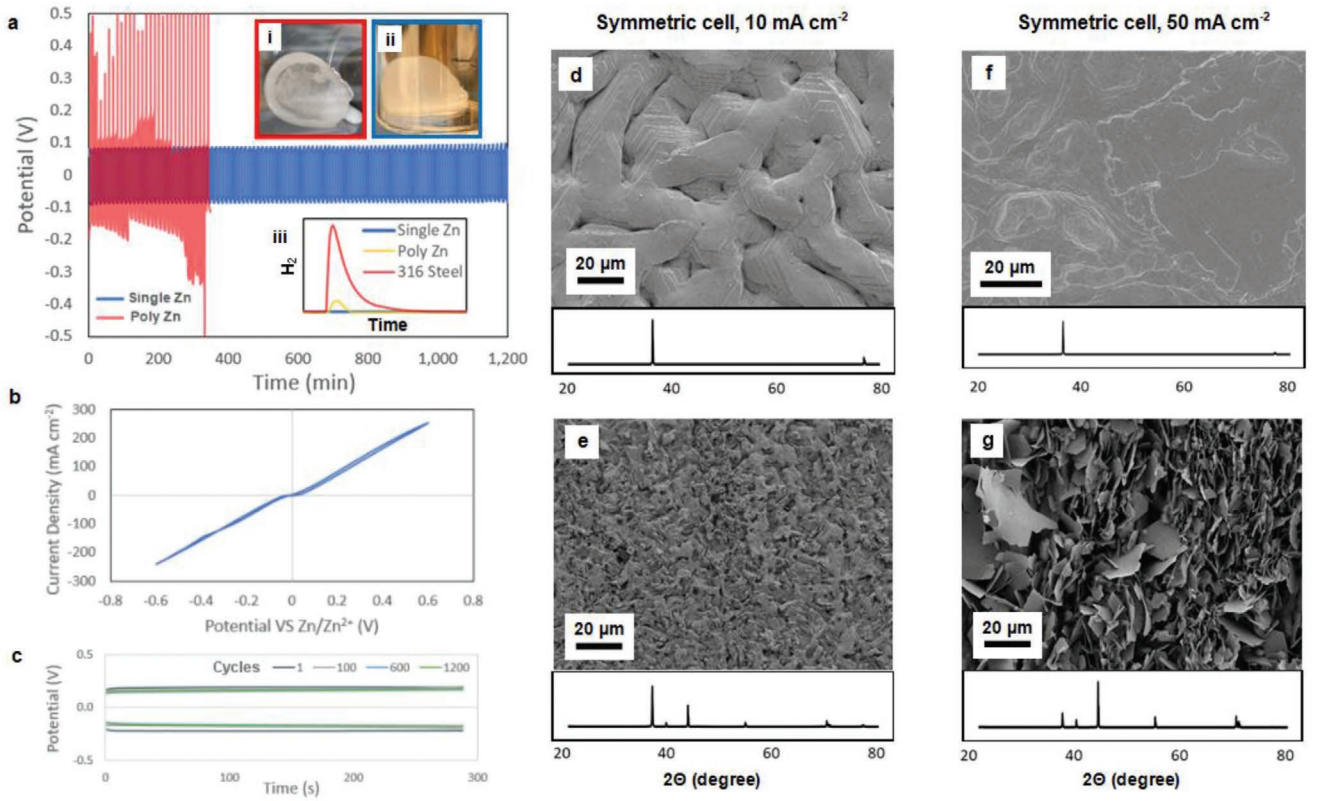

Figure 4. Cell cycling performance. a) Galvanostatic cycling of a Poly-Zn/stainless-steel cell (red) and a Single-Zn symmetric cell (blue) at 10 mA cm^{-2}. Insets: i) The Poly-Zn/stainless-steel cell separator, with significant "dead Zn" accumulation (dark areas). ii) The Single-Zn symmetric cell separator. iii) Online mass spectrometry of hydrogen evolution from the cycled separators following titration with H_2SO_4 solution. b) Cyclic voltammetry of a three-electrode cell (Single-Zn working electrode, Poly-Zn counter and reference electrodes) from –0.6 to +0.6 V versus Zn/Zn^{2+} at a scan rate of 20 mV s^{-1}. c) Cycling plots of plating and stripping overpotentials from a symmetric Single-Zn cell cycled for 1200 cycles at 50 mA cm^{-2} with 4 mAh cm^{-2} per-cycle capacity. d,e) SEM images and accompanying XRD spectra of the Single-Zn anode (d) and the Poly-Zn anode (e) after 100 cycles at 10 mA cm^{-2}, 1 mAh cm^{-2} per cycle. f,g) SEM and XRD spectra of the Single-Zn anode after 1200 cycles at 50 mA cm^{-2}, 4 mAh cm^{-2} per cycle (f), and the Poly-Zn anode after 200 cycles at 50 mA cm^{-2}, 1 mAh cm^{-2} per cycle (g).

Figures S8, S13, Supporting Information), XRD (Figure 4d, inset), and Fourier transform infrared (FTIR) spectroscopy (Figure S14, Supporting Information) results showing no formation of other components even after cycling. It was found that the Single-Zn underwent a loss of only 3.73 mg cm^{-2} after 1200 cycles, equivalent to an average 0.0025 mAh cm^{-2} capacity loss per cycle. This translates to an average CE over 1200 cycles of 99.94%, evidencing its excellent stability and reversibility. In comparison, when cycled under the same rate and at a lower capacity of 1 mAh cm^{-2} per cycle, a Poly-Zn symmetric cell's anode exhibited a highly flaky morphology after cycling (Figure 4g) and suffered from a more significant mass loss of 1.446 mg cm^{-2} after just 100 cycles, which translates to a much lower average CE of 98.8%.

To ensure its compatibility with conventional AZB cathodes, we have also assessed the cycling performance of the Single-Zn anode in a full cell, paired with a α-MnO_2 cathode at a current density of 5 mA cm^{-2}. After some initial turbulence in the first 20 cycles due to the cathode's unstable utilization rate and degradation, the discharge capacity gradually stabilized and maintained a 92% capacity retention after 250 cycles and an average CE of 99.85% (Figure S15a,b, Supporting Information). SEM imaging and XRD revealed the planar surface of the zinc anode was largely preserved after cycling (Figure S15c, Supporting Information). Occasional hexagonal pits were observed across the anode surface where Zn was removed to compensate for Zn ion loss due to cathode degradation during cycling, as the MnO_2 cathode does not itself possess a compensating Zn ion source.

In addition to its excellent cycling performance, we also found that the Single-Zn anode suppresses unwanted side reactions—corrosion and hydrogen generation reactions—commonly seen in AZBs during aging.[51,52] A stainless-steel and a Single-Zn anode were both electroplated with Zn from 2 M $ZnSO_4$ to a capacity of 8 mAh cm^{-2} and left to age in the same electrolyte under ambient conditions (Figure S16a–c, Supporting Information, left vial stainless steel, right vial Single-Zn). Bubble formation and discoloration can be readily observed from the stainless-steel anode even right after plating, which are indicative of metal corrosion and hydrogen generation. This worsened over time, with extensive bubble formation seen around the whole stainless-steel anode after 12 h of aging. After two days of aging, evidence of plated Zn delaminating from the steel anode due to the aggressive hydrogen gas generation was observed (Figure S16d, Supporting Information). Such Zn detachment into inactive "dead Zn" would reduce cell capacity.

By comparison, Zn plated onto the Single-Zn anode showed minimal discoloration throughout the aging process, and experienced much less bubble formation. We attribute the Single-Zn anode's robustness to aging to its flat electroplating morphology, minimizing the exposed surface area for side reactions to occur upon, and the elimination of the formation of other crystal orientations like (100), (101), and (110), which have been reported to be more susceptible to corrosion.[32] Whereas Zn plated on stainless steel presents a significantly rougher structure with various crystal orientations exposed to the electrolyte, making it more vulnerable to corrosion attack. However, Single-Zn was not completely immune to aging side reactions, with some discoloration observed, and XPS revealing additional chemical species indicative of some oxide and hydroxide formation on the metal surface (Figure S17, Supporting Information).

Other than serving as a high-performance AZB anode, this high-rate epitaxial electrodeposition system could also be used as a scalable method to grow Zn single crystals, which we believe can significantly reduce their current cost. The most widely used approach for commercial Zn-metal production is the Roast-Leach Electrowin (RLE) process, with Zn metal produced via the electrolysis of purified $ZnSO_4$ solution, itself made from roasting and leaching ZnS-containing ore. The RLE process could be readily modified for Single-Zn production (Figure S18, Supporting Information). To test this hypothesis, a significant amount of Zn (0.52 mm thickness, equivalent to 304 mAh cm^{-2} capacity) was electroplated onto the Single-Zn substrate at a rate of 30 mA cm^{-2} from $ZnSO_4$ solution. Planar Zn crystal with well-defined hexagonal shapes can be clearly resolved from the top surface of the electroplated Zn (**Figure 5**a), which indicates that the (002) crystal orientation was well maintained and the metallic Zn was plated epitaxially. This is further confirmed with XRD, which shows no new peak had emerged after cycling (Figure 5a, inset), and with extended-field-of-view EBSD (Figure S19, Supporting Information), with the uniformly colored mapping indicating that the plated metal Zn only possessed a single crystal orientation.

Attenuation contrast X-ray computed tomography (XCT) was employed to check the internal quality of the thick electroplated Zn layer (Figure 5b–d). The 3D rendered XCT image and the accompanying 2D image slices taken parallel to 5, 260, 520, and 700 µm beneath the interface reveal the morphology inside of the sample bulk (Figure 5b). It is shown that the bulk Zn deposition was free of large defects and showed no difference to the substrate Zn itself, apart from the sporadic grooves in close proximity to the plated Zn surface, which are likely the residual unclosed gaps between individual plated Zn islands. Virtual cross-sectional image slices resolved no interfacial defects or inhomogeneities between the substrate Zn and plated Zn (Figure 5c), suggesting the excellent epitaxial nature of the

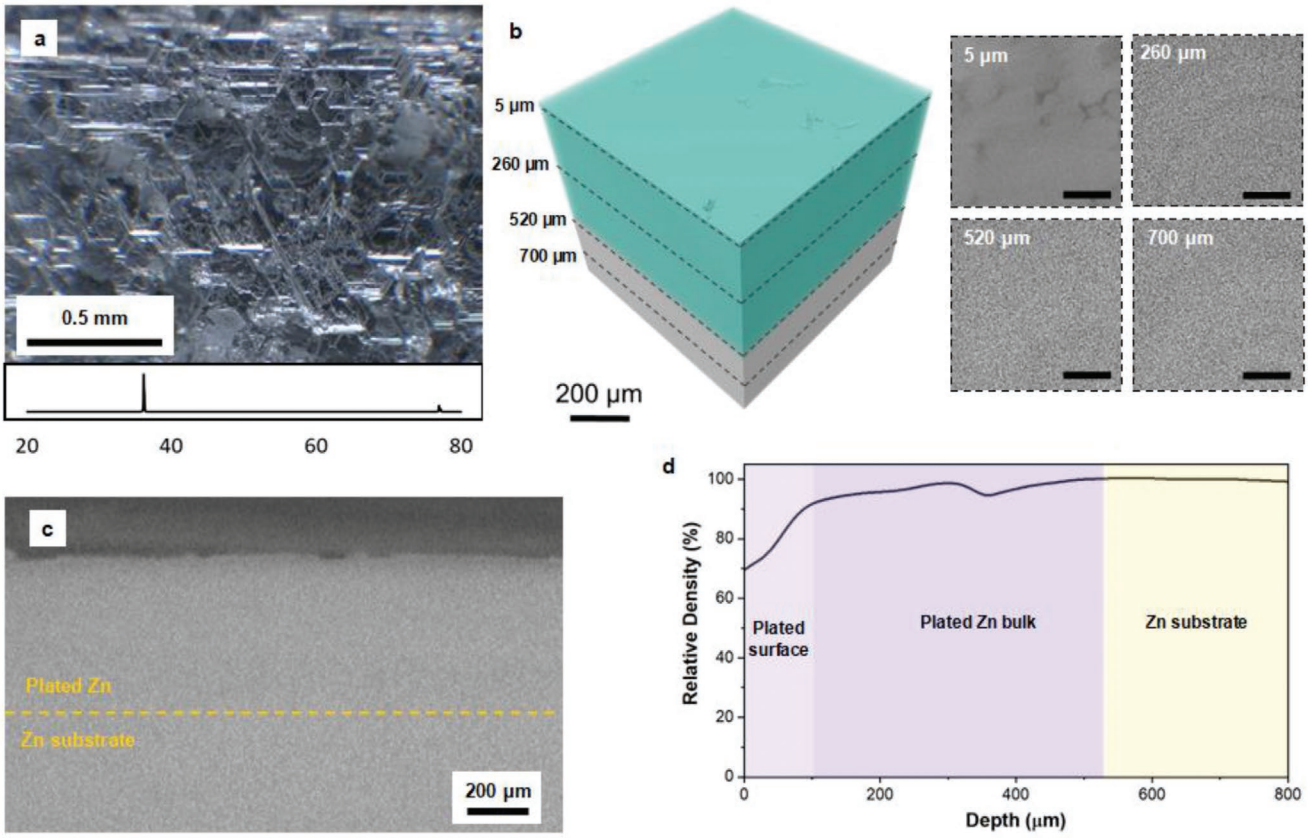

Figure 5. High-depth Zn electroplating to Single-Zn. a) Optical microscopy image and XRD of the Single-Zn surface following Zn electroplating to 0.41 mm depth. b) Volume-rendered XCT image of the plated Zn and Single-Zn substrate, with parallel 2D slices extracted at different depths from the surface (5, 260, 520, and 700 µm). The lower gray region indicates the substrate, the upper turquoise area the plated Zn. Scale bars: 200 µm. c) Virtual cross-sectional image slice of the plated Zn interface with the Single-Zn substrate. d) Calculated relative density profile over the volume in (b).

electroplating with defect-free metallic bonding. An average grayscale profile of the volume rendered 0.88 × 0.88 mm^2 region from the plated surface to inside the substrate was performed to examine the relative density of plated Zn, as detailed in the methods. Apart from the region close to the plated surface (<100 μm), where Zn island mergence may be incomplete, the bulk of the plated Zn shares comparable grayscale intensities with the 100 % dense substrate Zn, suggesting the electroplated Zn has perfect crystallinity with minimal voids formation (Figure 5d). A small dip in attenuation can be observed around 360 μm beneath the surface. We attribute this localized dip in density to relatively more inhomogeneous nucleation occurring at the start of plating, when the overpotential will be highest.[20,53] Overall, these results confirmed that single crystal Zn can be densely produced with no significant interior defects by epitaxial electrodeposition. The resultant single crystal Zn is of high quality, comparable to commercial crystals produced via the Czochralski method,[54] which confirmed this method can potentially be further developed for making good quality single crystals at a much lower cost.

3. Conclusion and Outlook

We have shown that, using only a suitable metallic anode, without any additional architecture, electrolyte, or interface modification,[1,4,35] the dendrite problem can be resolved and excellent cell performance can be achieved in AZBs. Using metallic Single-Zn as the anode, excellent planar, and dendrite-free Zn electrodeposition can be achieved at an unprecedented high rate of 200 mA cm^{-2}. And this dendrite-free epitaxial surface is well maintained after prolonged cycling (>1200 cycles) at 50 mA cm^{-2} with a per-cycle capacity of 4 mAh cm^{-2}. We attribute the excellent performance to the near-complete suppression of defect formation during electroplating, minimizing the availability of nucleation sites for dendrite formation, even when cycled under high rates. This presents a new strategy to preventing dendrites in aqueous zinc batteries and potentially in other battery systems as well.[47,55–58] We also demonstrated that epitaxial electrodeposition can be used as a simple and scalable method to grow high-quality Zn single crystals, which substantially lowers its cost. Our findings present a reliable strategy for solving one of the fundamental challenges in AZBs—dendrite growth at the metal anode—and if partnered with a suitably robust cathode[50,59–66] would yield a compelling high-rate, safe, and economic grid-level storage capability.

Supporting Information

Supporting Information is available from the Wiley Online Library or from the author.

Acknowledgements

A.W.R. thanks the support of the Royal Society. P.G.B. is indebted to the Engineering and Physical Sciences Research Council (EPSRC), including Henry Royce Institute for Advanced Materials and the Faraday Institution for financial support. The X.C.T. was facilitated by EPSRC grant EP/M02833X/1. The Zeiss Crossbeam FIB/SEM was supported by EPSRC grant EP/N010868/1. The authors thank the support and acknowledge the use of the facilities of the DCCEM, at the Materials Department, Oxford (EP/R010145/1).

Conflict of Interest

The authors declare no conflict of interest.

Author Contributions

S.D.P. and C.G. contributed equally to this work. S.D.P. conceived the idea and initial project plan. S.D.P. and C.G. led sample preparation and electrochemistry experiments. X.G., P.G.B., and A.W.R. directed the project and drafting the manuscript. C.G. led online MS measurements and analysis. Y.T.T. and R.C.R. led EBSD measurement and supported sample preparation. Z.N., B.H., and T.J.M. led XCT measurements and analysis. J.L. led FIB-SEM cross-section imaging. S.Z. led AFM measurements and analysis. J.-J.M. and L.P. led XRD and analysis. Y.Y. and S.C.E.T. prepared the cathode materials. Z.L. prepared electrolytes. D.M., M.J., and B.L. supported the SEM imaging, electrochemistry measurements, and sample preparation.

Data Availability Statement

The data that support the findings of this study are available from the corresponding author upon reasonable request.

Keywords

electroplating, zinc-metal anodes, zinc rechargeable batteries

Received: March 19, 2022
Revised: April 21, 2022
Published online:

[1] J. Shin, J. Lee, Y. Park, J. W. Choi, *Chem. Sci.* **2020**, *11*, 2028.
[2] G. Fang, J. Zhou, A. Pan, S. Liang, *ACS Energy Lett.* **2018**, *3*, 2480.
[3] H. Jia, Z. Wang, B. Tawiah, Y. Wang, C. Y. Chan, B. Fei, F. Pan, *Nano Energy* **2020**, *70*, 104523.
[4] M. Song, H. Tan, D. Chao, H. J. Fan, *Adv. Funct. Mater.* **2018**, *28*, 1802564.
[5] L. E. Blanc, D. Kundu, L. F. Nazar, *Joule* **2020**, *4*, 771.
[6] D. Alloyeau, W. Dachraoui, Y. Javed, H. Belkahla, G. Wang, H. Lecoq, S. Ammar, O. Ersen, A. Wisnet, F. Gazeau, *Nano Lett.* **2015**, *15*, 2574..
[7] *Surface and Interface Science*, (Ed.: K. Wandelt), Wiley-VCH, Weinheim, Germany **2013**.
[8] Q. Yang, G. Liang, Y. Guo, Z. Liu, B. Yan, D. Wang, Z. Huang, X. Li, J. Fan, C. Zhi, *Adv. Mater.* **2019**, *31*, 1903778.
[9] V. Yufit, F. Tariq, D. S. Eastwood, M. Biton, B. Wu, P. D. Lee, N. P. Brandon, *Joule* **2019**, *3*, 485.
[10] S. J. Banik, R. Akolkar, *J. Electrochem. Soc.* **2013**, *160*, D519..
[11] T. Otani, Y. Fukunaka, T. Homma, *Electrochim. Acta* **2017**, *242*, 364.
[12] Z. Liu, T. Cui, G. Pulletikurthi, A. Lahiri, T. Carstens, M. Olschewski, F. Endres, *Angew. Chem., Int. Ed.* **2016**, *55*, 2889.

[13] J. Abdulla, J. Cao, D. Zhang, X. Zhang, C. Sriprachuabwong, S. Kheawhom, P. Wangyao, J. Qin, *ACS Appl. Energy Mater.* **2021**, *4*, 4602.
[14] A. Bayaguud, X. Luo, Y. Fu, C. Zhu, *ACS Energy Lett.* **2020**, *5*, 3012.
[15] X. Guo, Z. Zhang, J. Li, N. Luo, G.-L. Chai, T. S. Miller, F. Lai, P. Shearing, D. J. L. Brett, D. Han, Z. Weng, G. He, I. P. Parkin, *ACS Energy Lett.* **2021**, *22*, 395.
[16] Z. Kang, C. Wu, L. Dong, W. Liu, J. Mou, J. Zhang, Z. Chang, B. Jiang, G. Wang, F. Kang, C. Xu, *ACS Sustainable Chem. Eng.* **2019**, *7*, 3364.
[17] Z. Yan, E. Wang, L. Jiang, G. Sun, *RSC Adv.* **2015**, *5*, 83781.
[18] J. F. Parker, C. N. Chervin, E. S. Nelson, D. R. Rolison, J. W. Long, *Energy Environ. Sci.* **2014**, *7*, 1117.
[19] H. He, H. Qin, J. Wu, X. Chen, R. Huang, F. Shen, Z. Wu, G. Chen, S. Yin, J. Liu, *Energy Storage Mater.* **2021**, *43*, 317.
[20] J. Zheng, L. A. Archer, *Sci. Adv.* **2021**, *7*, eabe0219.
[21] X. Jia, C. Liu, Z. G. Neale, J. Yang, G. Cao, *Chem. Rev.* **2020**, *120*, 7795.
[22] X. Wang, J. Meng, X. Lin, Y. Yang, S. Zhou, Y. Wang, A. Pan, *Adv. Funct. Mater.* **2021**, *31*, 2106114.
[23] M. Zhou, S. Guo, J. Li, X. Luo, Z. Liu, T. Zhang, X. Cao, M. Long, B. Lu, A. Pan, G. Fang, J. Zhou, S. Liang, *Adv. Mater.* **2021**, *33*, 2100187.
[24] J. Zheng, Y. Deng, J. Yin, T. Tang, R. Garcia-Mendez, Q. Zhao, L. A. Archer, *Adv. Mater.* **2022**, *34*, 2106867.
[25] S. Jin, D. Zhang, A. Sharma, Q. Zhao, Y. Shao, P. Chen, J. Zheng, J. Yin, Y. Deng, P. Biswal, L. A. Archer, *Small* **2021**, *17*, 2101798.
[26] D. Yuan, J. Zhao, H. Ren, Y. Chen, R. Chua, E. T. J. Jie, Y. Cai, E. Edison, W. Manalastas, M. W. Wong, M. Srinivasan, *Angew. Chem., Int. Ed.* **2021**, *60*, 7213.
[27] R. Yao, L. Qian, Y. Sui, G. Zhao, R. Guo, S. Hu, P. Liu, H. Zhu, F. Wang, C. Zhi, C. Yang, *Adv. Energy Mater.* **2022**, *12*, 2102780.
[28] J. Zheng, Q. Zhao, T. Tang, J. Yin, C. D. Quilty, G. D. Renderos, X. Liu, Y. Deng, L. Wang, D. C. Bock, C. Jaye, D. Zhang, E. S. Takeuchi, K. J. Takeuchi, A. C. Marschilok, L. A. Archer, *Science (80-.).* **2019**, *366*, 645.
[29] T. Foroozan, V. Yurkiv, S. Sharifi-Asl, R. Rojaee, F. Mashayek, *ACS Appl. Mater. Interfaces* **2019**, *11*, 44077.
[30] S. Li, J. Fu, G. Miao, S. Wang, W. Zhao, Z. Wu, Y. Zhang, X. Yang, *Adv. Mater.* **2021**, *33*, 2008424.
[31] J. Cao, D. Zhang, C. Gu, X. Wang, S. Wang, X. Zhang, J. Qin, Z. S. Wu, *Adv. Energy Mater.* **2021**, *11*, 2101299.
[32] K. E. K. Sun, T. K. A. Hoang, T. N. L. Doan, Y. Yu, X. Zhu, Y. Tian, P. Chen, *ACS Appl. Mater. Interfaces* **2017**, *9*, 9681.
[33] C. Lu, H. Zhou, *Sci. Bull.* **2020**, *65*, 1524.
[34] M. Rashad, M. Asif, Y. Wang, Z. He, I. Ahmed, *Energy Storage Mater.* **2020**, *25*, 342.
[35] B. Tang, L. Shan, S. Liang, J. Zhou, *R. Soc. Chem.* **2019**, *12*, 3288.
[36] J. Hao, X. Li, S. Zhang, F. Yang, X. Zeng, S. Zhang, G. Bo, C. Wang, Z. Guo, *Adv. Funct. Mater.* **2020**, *30*, 2001263.
[37] Y. Cheng, X. Xi, D. Li, X. Li, Q. Lai, H. Zhang, *RSC Adv.* **2015**, *5*, 1772.
[38] M. Bockelmann, U. Kunz, T. Turek, *Electrochem. Commun.* **2016**, *69*, 24.
[39] V. N. Perevezentsev, V. V. Rybin, V. N. Chuvil'deev, *Acta Metall. Mater.* **1992**, *40*, 895.
[40] B. Kuhr, D. Farkas, I. M. Robertson, D. Johnson, G. Was, *Metall. Mater. Trans. A Phys. Metall. Mater. Sci.* **2020**, *51*, 667.
[41] B. N. Singh, S. J. Zinkle, *J. Nucl. Mater.* **1993**, *206*, 212.
[42] B. P. Uberuaga, L. J. Vernon, E. Martinez, A. F. Voter, *Sci. Rep.* **2015**, *5*, 9095.
[43] J. Steiger, D. Kramer, R. Mönig, *J. Power Sources* **2014**, *261*, 112.
[44] K. J. Harry, D. T. Hallinan, D. Y. Parkinson, A. A. MacDowell, N. P. Balsara, *Nat. Mater.* **2014**, *13*, 69.
[45] Z. Zhao, J. Zhao, Z. Hu, J. Li, J. Li, Y. Zhang, C. Wang, G. Cui, *Energy Environ. Sci.* **2019**, *12*, 1938.
[46] C. Gong, S. D. Pu, X. Gao, S. Yang, J. Liu, Z. Ning, G. J. Rees, I. Capone, L. Pi, B. Liu, G. O. Hartley, J. Fawdon, J. Luo, M. Pasta, C. R. M. Grovenor, P. G. Bruce, A. W. Robertson, *Adv. Energy Mater.* **2021**, *11*, 2003118.
[47] S. D. Pu, C. Gong, X. Gao, Z. Ning, S. Yang, J. J. Marie, B. Liu, R. A. House, G. O. Hartley, J. Luo, P. G. Bruce, A. W. Robertson, *ACS Energy Lett.* **2020**, *5*, 2283.
[48] J. Xiao, Q. Li, Y. Bi, M. Cai, B. Dunn, T. Glossmann, J. Liu, T. Osaka, R. Sugiura, B. Wu, J. Yang, J. G. Zhang, M. S. Whittingham, *Nat. Energy* **2020**, *5*, 561.
[49] A. Konarov, N. Voronina, J. H. Jo, Z. Bakenov, Y. K. Sun, S. T. Myung, *ACS Energy Lett.* **2018**, *3*, 2620.
[50] H. Pan, Y. Shao, P. Yan, Y. Cheng, K. S. Han, Z. Nie, C. Wang, J. Yang, X. Li, P. Bhattacharya, K. T. Mueller, J. Liu, *Nat. Energy* **2016**, *1*, 16039.
[51] T. Hurlen, K. Schrøder, R. Havanka, T. Briggs, G. A. D. Haslewood, H. Flood, *Acta Chem. Scand.* **1962**, *16*, 1346.
[52] C. Li, X. Xie, S. Liang, J. Zhou, *Energy and Environmental Materials*, John Wiley & Sons, Ltd, Hoboken, NJ, USA **2020**, pp. 146–159.
[53] M. Chamoun, B. J. Hertzberg, T. Gupta, D. Davies, S. Bhadra, B. Van Tassell, C. Erdonmez, D. A. Steingart, *NPG Asia Mater.* **2015**, *7*, e178.
[54] *Handbook of Crystal Growth*, 2nd ed., Vol. *1,* (Ed.: T. Nishinaga), Elsevier, **2014**, https://doi.org/10.1016/C2011-0-04376-4.
[55] X. Gao, Y. N. Zhou, D. Han, J. Zhou, D. Zhou, W. Tang, J. B. Goodenough, *Joule* **2020**, *4*, 1864.
[56] Z. Ning, D. S. Jolly, G. Li, R. De Meyere, S. D. Pu, Y. Chen, J. Kasemchainan, J. Ihli, C. Gong, B. Liu, D. L. R. Melvin, A. Bonnin, O. Magdysyuk, P. Adamson, G. O. Hartley, C. W. Monroe, T. J. Marrow, P. G. Bruce, *Nat. Mater.* **2021**, *20*, 1121.
[57] B. Lee, E. Paek, D. Mitlin, S. W. Lee, *Chem. Rev.* **2019**, *119*, 5416.
[58] R. Davidson, A. Verma, D. Santos, F. Hao, C. Fincher, S. Xiang, J. Buskirk, K. Van; Xie, M. Pharr, P. P. Mukherjee, S. Banerjee, *ACS Energy Lett.* **2019**, *4*, 375.
[59] F. Wan, L. Zhang, X. Dai, X. Wang, Z. Niu, J. Chen, *Nat. Commun.* **2018**, *9*, 1656.
[60] Y. Dong, M. Jia, Y. Wang, J. Xu, Y. Liu, L. Jiao, N. Zhang, *ACS Appl. Energy Mater.* **2020**, *3*, 11183.
[61] G. Yang, Q. Li, K. Ma, C. Hong, C. Wang, *J. Mater. Chem. A* **2020**, *8*, 8084.
[62] J. Hao, B. Li, X. Li, X. Zeng, S. Zhang, F. Yang, S. Liu, D. Li, C. Wu, Z. Guo, *Adv. Mater.* **2020**, *32*, 2003021.
[63] V. Soundharrajan, B. Sambandam, S. Kim, M. H. Alfaruqi, D. Y. Putro, J. Jo, S. Kim, V. Mathew, Y. K. Sun, J. Kim, *Nano Lett.* **2018**, *18*, 2402.
[64] N. Zhang, F. Cheng, Y. Liu, Q. Zhao, K. Lei, C. Chen, X. Liu, J. Chen, *J. Am. Chem. Soc.* **2016**, *138*, 12894.
[65] W. Xiong, D. Yang, T. K. A. Hoang, M. Ahmed, J. Zhi, X. Qiu, P. Chen, *Energy Storage Mater.* **2018**, *15*, 131.
[66] V. Verma, S. Kumar, W. Manalastas, M. Srinivasan, *ACS Energy Lett.* **2021**, *6*, 1773.